Article:
Skelton, R and Walker, AM orcid.org/0000-0003-3121-3255 (2019) Interactions between bare and protonated Mg vacancies and dislocation cores in MgO. Physics and Chemistry of Minerals, 46 (5). pp. 471-485. ISSN 0342-1791

https://doi.org/10.1007/s00269-018-01017-7

Interactions between bare and protonated Mg vacancies and dislocation cores in MgO

Richard Skelton [a,*] and Andrew M. Walker[b]

[a] Research School of Earth Sciences, Australian National University, Canberra, ACT, 0200, Australia

(ORCID: 0000-0003-1583-2312)

[b] School of Earth and Environment, University of Leeds, Leeds, LS2 9JT, UK

(ORCID: 0000-0003-3121-3255)

* Corresponding author: richard.skelton@anu.edu.au

Abstract

Water can be incorporated into the lattice of mantle minerals in the form of protons charge-balanced by the creation of cation vacancies. These protonated vacancies, when they interact with dislocations, influence strain rates by affecting dislocation climb, pinning the dislocation, and, potentially, by altering the Peierls barrier to glide. We use atomic scale simulations to investigate segregation of Mg vacancies to atomic sites within the core regions of dislocations in MgO. Energies are computed for bare and protonated Mg vacancies occupying atomic sites close to ½<110> screw dislocations, and ½<110>{100} and ½<110>{110} edge dislocations. These are compared with energies for equivalent defects in the bulk lattice to determine segregation energies for each defect. Mg vacancies preferentially bind to ½<110>{100} edge dislocations, with calculated minimum segregation energies of -3.54 eV for $V_{Mg}^{''}$ and -4.56 eV for $2H_{Mg}^{x}$. The magnitudes of the minimum segregation energies calculated for defects binding to ½<110>{110} edge or ½<110> screw dislocations are considerably lower. Interactions with the dislocation strain field lift the 3-fold energy degeneracy of

the $2H_{Mg}^{x}$ defect in MgO. These calculations show that Mg vacancies interact strongly with dislocations in MgO, and may be present in sufficiently high concentrations to affect dislocation mobility in both the glide- and climb-controlled creep regimes.

Keywords: MgO; dislocation; cation vacancy; atomic-scale modeling

1. Introduction

Periclase (MgO, space group *Fm*-3*m*) is the Mg end-member of the ferropericlase solid solution, (Mg,Fe)O, the second most abundant mineral in the Earth's lower mantle. Ferropericlase is thought to accommodate the majority of the strain in the deforming lower mantle (Madi et al., 2005; Girard et al., 2016). It has been proposed, on the basis of theoretical calculations (Karki et al., 1999) and experimental measurements of its elastic properties (Marquardt et al., 2009), that ferropericlase is the primary contributor to the observed seismic wave anisotropy in this region. This seismic anisotropy is made possible by the development of crystal preferred orientation (CPO) in ferropericlase during deformation in the dislocation creep regime (Long et al., 2006). Dislocations are linear topological defects in crystals which act as carriers of plastic strain. Dislocation cores are regions of high strain, and can act as sinks for vacancies, impurities, and other point defects, an effect which is more pronounced around edge than screw dislocations (Bilby, 1950). Impurity atoms can modify the atomic structures of the dislocations to which they bind, as in the case of ½<111> screw dislocations in body centered cubic (bcc) Fe (Ventelon et al., 2015). They can affect dislocation mobility, either impeding dislocation glide through attractive elastic interactions between the dislocation and immobile impurities (Cottrell and Bilby, 1949), or enhancing it by reducing the Peierls barrier to glide (e.g Ashbee and Yust, 1982; Lauzier et al., 1989; Lu and Kaxiras, 2002).

In nominally anhydrous minerals (NAMs), water is commonly incorporated as H^+ in point defects, particularly cation vacancies, with concentration often expressed in ppm of water by weight, or the atomic ratio $H/10^6Si$. In MgO, typical substitution mechanisms involve the partial or full protonation of a vacancy defect, replacing a divalent cation M^{2+} (e.g. Mg^{2+}, Fe^{2+}) with a single proton $\{H_M\}^{\cdot}$, charge balanced by a trivalent impurity, or as neutrally-charged pair of protons, $2H_{Mg}^{x}$. *Ab initio* calculations show that the protonation of existing vacancies is highly exothermic (de Leeuw, 2001). The solubility of hydrogen in MgO is very low, and measured solubilities are <10 wt ppm H_2O (e.g. Bolfan-Casanova et al., 2000; Joachim et al. 2012). While the solubility of hydrogen is higher in ferropericlase than in pure MgO, hydrogen remains a trace element, with a reported solubility at 25 GPa of ~20 wt ppm in $(Mg_{0.93}Fe_{0.07})O$ (Bolfan-Casanova et al., 2002).

Atomistic calculations have shown that bare vacancies bind to ½<110>{110} edge dislocation cores (Puls, 1980, 1983). Although interactions between protonated vacancies and dislocation cores in MgO have not been similarly studied, both bare and protonated vacancies are known to segregate to grain boundaries in MgO (Verma and Karki, 2010; Karki et al., 2015). The presence of vacancy-related defects near dislocations may influence strain rates, especially under conditions of low temperature or high stress, where deformation is controlled by dislocation glide. High-stress experiments have found that the incorporation of protonated defects (often referred to as "water") in $(Mg,Fe)_2SiO_4$ olivine may reduce the Peierls stress by up to a factor of two (Katayama and Karato, 2008), and Peierls-Nabarro modeling suggests that protonated vacancies may have a similar effect on the Peierls stress of dislocations in MgO (Skelton and Walker, 2018). Recent measurements of seismic attentuation in Fo90 olivine under oxidizing conditions demonstrated that bare cation site vacancies produced to charge balance the oxidation of Fe^{2+} to Fe^{3+} can have similar effects on the mechanical properties of mantle minerals as protonated vacancies (Cline et al., 2018).

While long-range interactions between point defects and dislocations can be understood on the basis of elasticity theory, segregation of impurities to dislocation cores is an inherently atomistic phenomenon, driven by the dislocation core structure. Although the clouds of impurities segregated to dislocation cores can be observed experimentally using atom probe tomography (e.g. Miller, 2006), routine measurements of this kind remain difficult because of the small length scales involved. This technique has recently been used to image trace element distributions around dislocations in zircon (Piazolo et al., 2016; Reddy et al., 2016). Atomistic modeling techniques, in contrast, permit easy treatment of atomic-scale phenomena. Several popular techniques exist for modeling the atomic-scale properties of dislocations. In the dislocation multipole approach, several dislocations are inserted into a simulation cell with periodic boundary conditions in three dimensions (3D; Ismail-Beigi and Arias, 2000; Cai et al., 2001). This approach makes possible the use of *ab initio* methods, such as density functional theory (DFT; Hohenberg and Kohn, 1964; Kohn and Sham, 1965), to calculate the energy of a dislocation. However, dislocation-dislocation interactions can modify the structure of the dislocation core, and a rigorous calculation of the energy of a single dislocation requires the elastic interactions between dislocations to be subtracted from the total energy (Cai et al., 2003). This approach has been described in detail by Carrez et al. (2015), where it was used to calculate the core structure and energy of ½<110> screw dislocations in MgO to lower mantle pressures.

An alternative is to embed a single dislocation in a cylindrical cluster of atoms, subject to periodic boundary conditions along the axis of the cylinder. This cluster is aperiodic normal to the dislocation line vector $\boldsymbol{\xi}$. In this approach, the cluster of atoms is divided radially into two regions: an inner cylinder (region I) where atoms are permitted to relax freely and an outer region (II) where they are held fixed at the locations predicted from elastic strain field of the dislocation. There are several limitations to this method: a large inner radius is required to fully converge the dislocation core

properties; the outer surface of the cluster may become charged when modeling ionic materials; and interactions between a moving dislocation and the surface separating region I from region II render accurate calculation of the Peierls stress σ_p difficult. Additionally, because the simulation cell includes surfaces, the core energy cannot easily be calculated using DFT, as the energy will include a component due to relaxation of the electron density at the surface. However, the absence of dislocation-dislocation interactions in the cluster-based approach, combined with its ease of implementation, has made it a valuable tool for simulating dislocations in ionic materials. A detailed exposition of the cluster-approach and its use in computational mineral physics may be found in Walker et al. (2005a). The cluster based method has been applied extensively to MgO, including to study the core structure and mobility of ½<110>{110} edge dislocations (Puls and Norgett, 1976), segregation of cation and anion vacancies to ½<110>{110} edge dislocation (Puls, 1980, 1983), pipe diffusion along ½<110>{110} edge dislocations (Zhang et al., 2010), the structure of surface-terminated ½<110> screw dislocations (McKenna, 2013), the core structure of <100> screw dislocations (Watson et al., 1999; Walker et al., 2005b). Dislocations in MgO have also been investigated using other computational methods, including the supercell approach (Carrez et al., 2015) and the semi-continuum Peierls-Nabarro-Galerkin method (Amodeo et al., 2011; Amodeo et al., 2012; Cordier et al., 2012).

In this paper, core structures and energies at 0 GPa are calculated using the cluster-based approach with the interatomic interactions modeled using empirical pair potentials for several important dislocations in MgO, including ½<110>{110} and ½<110>{100} edge dislocations, and screw dislocations with Burgers vector ½<110>. Energies for segregation of vacancy-related point defects to each dislocation are calculated. For each dislocation type, we take the lowest energy core structure and calculate the energies of bare and protonated Mg vacancies, written $V_{Mg}^{''}$ and $2H_{Mg}^{x}$ in

Kröger-Vink notation (Kröger and Vink, 1956), occupying cation sites near the dislocation line. Segregation energies are then calculated by comparing these energies with those of equivalent point defects in the bulk crystal, to determine the strength of the binding interactions between Mg vacancies and the dislocation core, and the influence that hydrogen has on these interactions.

2. Computational methods

2.1 Cluster-based simulation of dislocations

In the cluster-based approach, a single dislocation is inserted along the axis of a cylinder of atoms, which is periodic in one dimension (1D), along the axis of the cylinder. The first step is to displace atoms according to the elastic displacement field $\mathbf{u}(\mathbf{r})$ calculated for the dislocation. Here, we use the sextic formulation for a dislocation in an anisotropic medium (Stroh, 1958). In this formulation, the displacement is assumed to take the form $\mathbf{u}(\mathbf{x}) = D_k\mathbf{A}_k\log(\eta_k)/2\pi i$,where the vectors $\mathbf{A}_k$ depend on the roots of a sextic polynomial. For edge dislocations, this is a non-conservative algorithm and atoms must be removed from the simulation cell to obtain a physically reasonable initial dislocation structure. To do this, a branch cut is created that is normal to both the Burgers and dislocation line vectors. Any atoms which are displaced across this branch cut by the displacement field $\mathbf{u}(\mathbf{r})$ are deleted. Atoms in close proximity to the branch cut are merged with any nearby atoms, if the distance between them falls below a specified threshold distance $d_{\min}$. Once the elastic displacement field has been applied to the cluster, it is divided into two concentric regions whose radii are r_{I} and r_{II}, respectively. During geometry optimization, the coordinates of atoms in region I are unconstrained, while the coordinates of atoms in region II are fixed. All simulations are performed at a constant pressure of 0 GPa and a temperature of 0 K, ignoring configurational entropy.

The total excess energy per unit length, E_{dis}, contained within radius r of an isolated dislocation is

$$E_{dis}(r) = E_{core} + \frac{Kb^2}{4\pi}\log(r/r_c) \qquad (1)$$

where K is the elastic energy coefficient, E_{core} is the energy contained within the core region (termed the core energy), and r_c is the radius of the dislocation core, within which the displacement field diverges from the predictions of linear elasticity. The core radius r_{c} is an undetermined parameter, whose value cannot determined from the radial excess energy of the dislocation. Its value must be chosen in order to set a gauge for the core energy. In this study, we use a core radius of $2b$, where b is the absolute magnitude of the Burgers vector. The elastic energy coefficient K is computed using the Stroh sextic theory (1958) during the calculation of the elastic displacement field. Its value depends on the anisotropic elastic constants C_{ij}, the Burger's vector **b**, and the dislocation line vector $\boldsymbol{\xi}$. For ½<110>{100} edge dislocations, K = 197.9 GPa, for ½<110>{110} edge dislocations, K = 182.8 GPa, and K = 136.9 GPa for ½<110> screw dislocations.

The core energy is determined from atomistic cluster-based simulations by fitting equation (1) to the calculated radial dependence of the excess energy, which is the difference between the energy of a cluster containing the dislocation and a reference system containing an identical number of atoms. E_{core} is also the excess energy of the dislocation at $r = r_c$. For screw dislocations, this is straightforward, as the undeformed and deformed simulation cells contain the same number of atoms. However, as the insertion of an edge dislocation is non-conservative (i.e. atoms are removed from the initial simulation cell), the excess energy must be calculated from the energies of the individual atoms as

$$E_{excess}(r) = E_{dis}(r) - \sum_{species} n_{species}(r) E_{species} \quad (2)$$

where $E_{dis}(r)$ is the total energy of the atoms within r of the dislocation line, the sum runs over the different atomic species present, $n_{species}(r)$ gives the number of atoms of each species within r, and E_{species} is the energy of the species in the bulk lattice. In multicomponent crystals, such as MgO, this is equal to

$$E_{species} = 1/2\left(E_{supercell} + E_{isolated} - E_{vac}\right) \quad (3)$$

where E_{vac} is the energy of a supercell from which one atom of the specified type has been removed, without relaxing the coordinates of the remaining atoms, $E_{supercell}$ is the energy of the supercell without a vacancy, and $E_{isolated}$ is the energy of an isolated atom of the specified type.

The core energy and core displacement field of a dislocation in a two-region cluster depends on the value of r_{I}, the radius of the relaxed region. Although the initial coordinates for all atoms are set using a purely elastic displacement field, atoms close the dislocation core experience a significant inelastic component of displacement due to atomic-scale relaxation near the dislocation core. Consequently, for small r_{I}, some component of the total displacement will be missed, leading to higher core energies than if all atoms were permitted to move during relaxation. For all dislocations examined in this study, values of r_{I} and r_{II} were chosen to ensure convergence, to within <25 meV/Å, of the E_{core} determined by fitting equation (1) to the calculated excess energy curve. For all three dislocation slip systems, region I and region II radii of 30 Å and 45 Å were sufficient to achieve this level of convergence.

In this study, we treat the interatomic interactions using the widely used potential model of Lewis and Catlow (Lewis and Catlow, 1985), with the hydroxyl groups modeled using the parameters developed by Schröder et al. (1992) to simulate $(OH)^-$ incorporation into zeolite, and subsequently modified by

Gatzemeier and Wright (2006) to better fit O-H stretching frequencies in pyroxene. It is capable of reproducing, with reasonable accuracy, generalized stacking fault energies calculated for Mg_2SiO_4 olivine using DFT (Mahendran et al., 2017). All atomistic calculations are performed using the molecular mechanics program GULP (Gale 1997; Gale and Rohl 2003), selected for its compatibility with shell model potentials. The Coulomb interaction is treated using the Wolf summation approach (Wolf et al. 1999). In all calculations, we use a damping factor of 0.2 and a cutoff radius of 15.0 Å, which is sufficient to guarantee convergence of the total cell energy and elastic constants C_{ij} of point defect-free MgO to <1% of the value calculated using the Ewald summation technique.

2.2 Modeling point defect segregation

The energy required to move a point defect from the bulk lattice to a site near a dislocation core is termed the segregation energy, $E_{seg.}$ In an atomistic simulation, this is equivalent to the difference between the excess energy ΔE_{dis} of a point defect of the specified type in a simulation cell containing a dislocation, and the excess energy ΔE_{perf} of the point defect in a 3D-periodic supercell of the material. Here, E_{seg} is calculated as

$$E_{seg} = \left(E_{dfct+dis} - E_{dis}\right) - \left(E_{dfct+supercell} - E_{supercell}\right) \quad (4)$$

where E_{dis} is the energy of a cluster containing a dislocation, $E_{dfct+dis}$ is the energy of that same cluster with a single point defect inserted, $E_{supercell}$ is the energy of a defect-free 3D-periodic supercell, and $E_{dfct+supercell}$ is the energy of a supercell containing a point defect. Negative segregation energies correspond to an attractive interaction between the point defect and dislocation core, and a correspondingly higher defect concentration than in the unstrained lattice. Conversely, point defects will not bind to sites for which the computed segregation energy is positive.

Due to the 1D periodic boundary conditions imposed on the simulation cell, each point defect interacts with periodic images of itself along the dislocation line. Consequently, calculating $E_{\mathrm{dfct+dis}}$ for a single point defect adsorbed to a dislocation core requires that the thickness of the 1D-periodic simulation cell along the dislocation line vector $\boldsymbol{\xi}$ be increased, which is done by stacking n simulation cells along $\boldsymbol{\xi}$. The value of n was checked to ensure that defect energies converged. For the ½<110>{100} edge and ½<110> screw dislocations, a stack thickness of n = 5 was used, giving a distance of 14.8 Å between a point defect and its nearest periodic image. Calculations for defects segregating to the ½<110>{110} edge dislocation used a cell thickness of n = 4, so that the shortest distance between adjacent point defects was ~16.8 Å. The 3D-periodic supercell used to calculate the excess energy of an isolated point defect in the bulk lattice must also be sufficiently large to minimize interactions between the point defect and its periodic images. For this purpose, a 4×4×4 simulation cell, for which the shortest distance between point defects is ~16.8 Å, was sufficient for convergence of the defect energy with same precision obtained for simulations of vacancy-dislocation interactions. Interactions between charged defects (i.e. $V_{Mg}^{''}$ defects) are corrected using the method of Leslie and Gillan (1985).

Due to the large size of the simulation cell and the $O(N^2)$ scaling of the Broyden-Fletcher-Goldfarb-Shanno (BFGS) algorithm (Shanno, 1970) used to minimize the dislocation energy, where N is the number of atoms permitted to relax, it is desirable to limit the computational cost by relaxing as few atomic coordinates as required to compute the energy to within the specified tolerance. However, the perturbation of the dislocation displacement field by the point defect is large only in the immediate vicinity of the point defect. Atoms outside this region may be fixed at the positions predicted for a dislocation without segregated point defects, without changing the calculated dislocation-point defect interaction energy significantly. In this study, all atoms a distance less than or equal to r from the

inserted point defect are allowed to move freely during relaxation. Due to the shorter range of the elastic field of a point defect, relative to a dislocation, *r* is smaller than the region I radius used to determine the dislocation core structure, reducing the number of atoms whose coordinates need to be relaxed. The calculated segregation energy is strictly decreasing with increasing relaxation radius, which must therefore be varied to test for convergence. For all dislocations and point defects considered in this study, the radius of the relaxed region is r = 10 Å, sufficient to converge the energies of the tightest binding sites to <0.05 eV.

Calculating the segregation energy of a bare Mg vacancy is straightforward, as this defect can be inserted into a simulation cell by deleting one of the Mg ions. Since $V_{Mg}^{''}$ is a charged defect, the calculated cell energy must be corrected for electrostatic interactions between the defect and its periodic images, as was done for equivalent defects in the bulk lattice environment. Setting up a segregation energy calculation is less straightforward if the vacancy is protonated, because the interatomic potential employed here models the oxygen ion in a hydroxyl group differently from other oxygen ions: with a partially ionic charge, and without a polarizable shell. Creating a protonated vacancy entails not only the removal of an Mg^{2+} ion and insertion of two H^{+} ions in the cation site, but also the replacement of two oxygen anions around the Mg site with oxygen ions tailored for membership of a hydroxyl group. Additionally, unlike a bare vacancy, a protonated defect has an orientation, defined by the direction of the O-H bond for which the defect energy is minimized. There are thus several symmetrically distinct configurations of the $2H_{Mg}^{x}$ defect for each site around a dislocation, corresponding to the different O-H bond orientations. Determining the minimum segregation energy for a $2H_{Mg}^{x}$ to a particular site in the dislocation core region entails calculating segregation energies for each of these configurations, as is done below.

3. Dislocation core properties

For each of the three dislocation slip systems considered in this study, there are multiple possible core structures, corresponding to the different high-symmetry locations in the appropriately oriented unit cell. These are shown in Fig. 1a for dislocations gliding on {110} and in Fig. 1b for dislocations gliding on {100}. To obtain stable structures for each of the three dislocation slip systems, radial excess energy profiles were calculated for dislocations centered at a number of different locations using the methods described above, and their core energies E_{core} extracted by fitting to equation (1). The locations shown in Fig. 1 have the lowest values of E_{core} from the set of cores considered in this study. Radial excess energies for the stable dislocation slip systems are shown in Fig. 2, together with the fitted excess energy curves $E(r)$.

All three dislocation types considered in this study were found to have multiple core structures, corresponding to different possible locations of the dislocation line within the unit cell (Fig 1ab), which have identical core energies. In this study, the ½<110>{110} edge dislocation was found to have two core structures with indistinguishable energies, both with fitted core energies of 1.35 eV/Å. For one such stable structure, the dislocation line is located along the channel parallel to <100> (site A in Fig. 1a). The other is centered on the column of alternating oxygen and magnesium ions parallel to the <100> lattice direction, and intersects the {100} plane (site B in Fig. 1a). In the discussion which follows, these two polymorphs are referred to as the <100>-channel-centered (Fig. 3a) and ion-centered (Fig 3b) structures, respectively. The predicted occurrence of energy degenerate core structures contrasts with previous theoretical studies, in which the ion-centered structure is reported to be the unique stable core structure (Zhang et al., 2010). This may attributable to the use of a breathing shell model by Zhang et al. (2010), which is more sophisticated than the Lewis and Catlow (1985) potential used in this study. However, it is worth noting that polymorphism of the ½<110>{110} edge

dislocation slip system has been observed in MgO bicrystals by transmission electron microscopy (Wang et al. 2014). The Nye tensor α_{ij}, which describes the distribution of dislocation density in a crystal and can be used to characterize the spreading of the dislocation core, is calculated here using the method of Hartley and Mishin (2005ab). Both polymorphs of the ½<110>{110} edge dislocation have undissociated cores, as the edge component α_{13} of the Nye tensor is unimodal (Fig. 3ab). However, the non-zero value of α_{23} indicates that the atoms are relaxed away from the glide plane due to shear-tension coupling, as described by Bulatov and Kaxiras (1997) for Si. The magnitude of the screw component α_{33} is negligible at all lattice points.

½<110>{100} edge dislocations similarly have two energy-degenerate core structures, one centered on the <110>-parallel column of oxygen anions (site C in Fig. 1b) and the other on the <110>-parallel column of Mg cations (site D in Fig. 1b), both of which have core energies of 1.91 eV/Å. In the discussion which follows, these two polymorphs are referred to as the O-centered (Fig. 3c) and Mg-centered (Fig. 3d) structures. In contrast to the ½<110>{110} edge dislocation, for which the two degenerate core structures differ significantly from one another, the O-centered and Mg-centered ½<110>{100} edge dislocation structures are nearly identical, except that the positions of the Mg and O ions are reversed. This can be easily seen by comparing the α_{13} and α_{23} components of the Nye tensor (Fig. 3de), which are visually indistinguishable. As it was found for ½<110>{110} edge dislocations, α_{23} is non-zero, indicating the presence of shear-tension coupling within the dislocation core, and the screw component α_{33} is effectively zero.

½<110> screw dislocations similarly have two degenerate core structures, each with a fitted core energy of 1.07 eV/Å. One of these core structures is centered on the <110>-oriented channel (site E in

Fig. 1b), while the second intersects the Mg-O bonds with non-zero projection onto the dislocation line (site F in Fig. 1b). These are labeled the <110>-channel-centered (Fig. 4a) and edge A-centered (Fig. 4b) core structures, respectively. The relative insensitivity of the core energy of the ½<110> screw dislocation to its origin in the unit cell agrees with the earlier calculations of Watson et al. (1999), who also calculated the core energy of the ½<110> screw dislocation to be 1.21 eV/Å (when corrected to the core radius used in this study). The screw component of the Nye tensor, α_{33}, is spread on the {110} plane (Fig. 4) for both stable core structures, consistent with the core spreading reported by Carrez et al. (2015) for this dislocation. Whereas the screw component α_{33} of the Nye tensor $\boldsymbol{\alpha}$ is zero for both edge dislocations in MgO, the edge components, α_{12} and α_{13}, are non-zero for the ½<110> screw dislocation, meaning that the displacement field for the ½<110> screw dislocation has a significant edge character.

The supercell method has previously been used to evaluate the core structure and energy of the ½<110> screw dislocation, with interatomic interactions simulated using a partially ionic rigid ion model of Henkelman et al. (2005), finding that the core energy is 1.10 eV/Å (Carrez et al., 2015), within error of the value calculated here. In contrast to this study, Carrez et al. (2015) predict that only the channel-centered structure is stable at 0 GPa, while the edge A-centered polymorph has a lower core energy at higher pressures. This may be a consequence of the relatively small cell size used by Carrez et al. (2015), as substantial dislocation-dislocation interactions may alter the core structure. Watson et al. (1999) also report, on the basis of cluster-based calculations, that the stable configuration of the MgO ½<110> screw dislocation is the channel-centered polymorph, and that dislocations inserted at other locations in the crystal structure will relax to this location. Although both studies find only a single stable core structure at 0 GPa, it is worth noting that this structure is one of the two low energy core structure polymorphs found in this study for the ½<110> dislocation.

Similarly, although Zhang et al. (2010) only report a single stable core structure for the ½<110>[110} edge dislocation, that structure (the ion-centered polymorph shown in Fig. 3b) is one of the two structures found to be stable in this study.

4. Segregation energies

4.1 Bare vacancy ($V_{Mg}^{''}$)

The tightest binding site for $V_{Mg}^{''}$ defects around a ½<110>{110} edge dislocation has a segregation energy of -1.51 eV (Fig. 5), comparable to the -1.5 eV calculated by Puls (1980), but slightly higher than the value of -1.7 eV found by Zhang et al. (2010) using a breathing shell potential. The tightest binding sites for both polymorphs of the dislocation core are located immediately above the dislocation line, which is consistent with the earlier calculations by Zhang et al. (2010). Spread out on the {110} plane directly below the dislocation line is an array of sites with low segregation energies (< -1.0 eV), which is consistent with the wide core spreading predicted for this dislocation by DFT-parameterized Peierls-Nabarro calculations (Amodeo et al., 2011) and visible in the α_{13} component of the Nye tensor (Fig. 3).

$V_{Mg}^{''}$ defects bind more tightly to lattice sites around ½<110>{100} edge dislocations, with maximum binding energies for the O-centered and Mg-centered polymorphs exceeding those calculated for the ½<110>{110} edge dislocation, by ~2 eV in the case of the Mg-centered polymorph (Fig. 6). Additionally, in contrast to the ½<110>{110} edge dislocation, segregation energies were found to differ markedly between the two polymorphs for the ½<110>{100} edge dislocation slip system, so that Mg vacancies bind more strongly to the core of the Mg-centered polymorph than the

O-centered polymorph. This suggests that the presence of Mg vacancies may stabilize the former core structure relative to the latter, lifting the energy degeneracy of the ½<110>{100} edge dislocation.

As the magnitudes of the strain fields around screw dislocation cores are, in general, less than those for similarly oriented edge dislocations, the binding energies calculated for Mg vacancies are lower for the ½<110> screw than for either of the edge dislocation slip systems. Nevertheless, as it can be seen in Table 1, binding energies are close to -1.0 eV, indicating moderately strong binding between V''_{Mg} defects and the screw dislocation core. The lowest energy sites are located close to the {110} plane normal to {100} glide plane (Fig. 7ab). This is likely a consequence of core spreading of ½<110> screw dislocations (Carrez et al., 2015), which is visible in the associated Nye tensor distribution α (Fig. 3). Semi-continuum Peierls-Nabarro-Galerkin calculations suggest that 80% of the dislocation core b_i is distributed on this plane (Amodeo et al., 2011).

4.2 Protonated vacancy ($2H^{x}_{Mg}$)

The H^+ ions in the most stable configuration of the $2H^{x}_{Mg}$ defect in MgO are bonded to O^{2-} ions on opposite sides of the MgO_6 octahedron, with the O-H bonds parallel and pointing towards the center of the site. Due to the high symmetry of the MgO unit cell, there are three possible symmetry-equivalent configurations of this defect, corresponding to the three pairs of opposing O^{2-} ions around the Mg site. However, the insertion of a dislocation into the MgO lattice breaks its rotational symmetry, and hence lifts the three-fold degeneracy of the $2H^{x}_{Mg}$ point defect. For both <110> and <100> oriented dislocations, this results in two symmetrically distinct defect structures, one of which is doubly degenerate.

We begin by considering the ½<110>{110} edge dislocations (Fig. 5). In the first of the two possible $2H_{Mg}^{x}$ configurations around this dislocation, the O-H bonds lie in the plane normal to the dislocation line **ξ**, oriented at 45° relative to the glide plane. Due to the mirror symmetry of the dislocation, this defect, referred to hereafter as HCROSS, is doubly degenerate. The second possible $2H_{Mg}^{x}$ configuration corresponds to the case when the O-H bonds are oriented parallel to the dislocation line, and will be referred to hereafter as the HPARA configuration. As shown in Table 1, the minimum segregation energy calculated for the HPARA defect is >1 eV lower than that calculated for the HCROSS defect. The mobility of hydrogen ions within a crystallographic site is high (Muir and Brodholt 2018), so that $2H_{Mg}^{x}$ defects can easily transform from a high to a low energy configuration when they occupy a site close to a dislocation line. This means that a $2H_{Mg}^{x}$ defect segregating to a ½<110>{110} dislocation will easily be polarized by the strain field induced by the dislocation, with the O-H bond vector oriented parallel to the dislocation line. Compared with bare Mg vacancies, $2H_{Mg}^{x}$ defects bind more tightly to the core of this dislocation, with energies up to ~0.5 eV lower than calculated for $V_{Mg}^{''}$ defects in the tightest binding site.

For $2H_{Mg}^{x}$ defects around ½<110>{100} edge dislocations, the two symmetrically distinct configurations are HPLANE, in which the O-H bond vectors lie within the {100} glide plane and are inclined at 45° with respect to **ξ**, and HNORM, in which the O-H bonds are parallel to the glide plane normal. Segregation energies are typically lower for the HPLANE configuration than the HNORM configuration, especially for sites close to the dislocation line (Fig. 6). The segregation energy of the tightest binding site for a $2H_{Mg}^{x}$ defect in the HPLANE configuration is lower than for the tightest binding site of the HNORM defect, by 1.25 eV in the case of the O-centered dislocation compared

with 1.60 eV for the Mg-centered dislocation. Echoing the behavior previously observed for $V_{Mg}^{''}$ defects, the calculated maximum $2H_{Mg}^{x}$ binding energies differ between the two ½<110>{100} edge dislocation core structure polymorphs, with lowest segregation energies calculated for sites near the Mg-centered core structure. $2H_{Mg}^{x}$ defects, like $V_{Mg}^{''}$ defects, bind more tightly to ½<110>{100} edge dislocations than ½<110>{110} edge dislocations, which may influence the relative mobilities of the ½<110>{100} and ½<110>{110} slip systems, particularly at low temperature or when the bulk concentration of Mg vacancy defects is low.

Generalized stacking fault energies, which can be used to parameterize a Peierls-Nabarro model for dislocation glide, are reduced in MgO by the presence of protonated vacancies at the slip plane (Skelton and Walker, 2018). However, this reduction depends on the orientation of the O-H bond, and glide is lubricated only by $2H_{Mg}^{x}$ defects whose O-H bond vectors are perpendicular to the glide plane normal (i.e. contained within the glide plane). For ½<110>{110} and ½<110>{100} edge dislocations, the configurations which are predicted to ease glide are the HPARA and HPLANE configurations (Skelton and Walker 2018). These defects have lower energies than configurations in which the O-H bond vectors have components parallel to the glide plane vector, as is required for $2H_{Mg}^{x}$ defects to ease glide of these dislocations.

The symmetrically distinct configurations of the $2H_{Mg}^{x}$ defect around a ½<110> screw dislocation are identical to those already described for the ½<110>{100} edge dislocation. In contrast to ½<110>{100} edge dislocations, where there is a sharp contrast in segregation energies between the two defects, the tightest binding sites for HNORM and HPARA defect configurations have comparable energies (Table 1), although the HPARA configuration is slightly more stable around the

edge A-centered polymorph, and vice-versa for the channel-centered polymorph. The difference between the minimum segregation energies for $V_{Mg}^{''}$ and $2H_{Mg}^{x}$ defects is even lower for screw dislocations than ½<110>{110} edge dislocations. Protonated vacancies are thus expected to be relatively low abundance around screw dislocations, except at high bulk $(OH)^{-}$ concentrations.

½<110> screw dislocations can glide on both the {110} or {100} planes, and the $2H_{Mg}^{x}$ defect configuration most suitable for lubricating glide will be different for the two planes. For glide on {100}, the O-H bonds in the HPLANE defect configuration lie within the glide plane, while HNORM is the preferred configuration for lubrication of {110} glide. However, although minimum segregation energies differ between the two defects, with the order depending on the core structure, energy differences are considerably smaller than those found for edge dislocations. It seems likely that the low energy sites spread along <100> are of greater significance for the preferred glide plane of ½<110> screw dislocations in hydrated MgO.

For ½<110>{110} edge dislocations and ½<110> screw dislocations, the calculated minimum segregation energies are essentially independent of the particular core structure, although in the case of the screw dislocation this is due to reconstruction of the dislocation core induced by the presence of a vacancy. However, calculated minimum segregation energies for $V_{Mg}^{''}$ and $2H_{Mg}^{x}$ defects around a ½<110>{100} edge dislocation are markedly different for the two polymorphic core structures of this dislocation. For both defect types, calculated minimum segregation energies are lowest for the Mg-centered polymorph. The energy difference is 0.35 eV for the low-energy planar configuration of the $2H_{Mg}^{x}$ defect and 0.7 eV for the $V_{Mg}^{''}$ defect. While the calculated segregation energy differences between the two polymorphs are relatively small in comparison with the total segregation energy, they represent a significant fraction of the core energy E_{core}.

Consequently, the energy degeneracy of the two polymorphic ½<110>{100} edge dislocation core structures is broken by the addition of vacancy-related defects, as segregation of these defects to Mg-centered dislocations is preferred. This can be easily explained by considering the strain field around a dislocation. For both polymorphs, the lowest energy site(s) lie below the glide plane. However, because the lowest energy site for the Mg-centered structure is directly below the dislocation line, it is closer to the center of the dislocation core than are either of the lowest energy sites for the O-centered dislocation, and thus relieves more strain in the Mg-centered structure than the O-centered one.

Enhancement of dislocation mobility in MgO driven by vacancy segregation is likely to be influenced by in pressure, temperature, and iron content, with implications for the mechanisms by which chemical environment alters the rheology of periclase in the lower mantle. If periclase is the load-bearing phase, this could alter the viscosity of the mantle. At high temperatures, configurational entropy will tend to favor increased relative vacancy concentrations in the bulk lattice, but concentrations of these point defects in dislocation core sites will remain elevated at mantle relevant temperatures. Increasing pressure decreases the core width of dislocations in MgO (Amodeo et al., 2012; Carrez et al., 2015). Vacancy segregation energies appear to be lowest in regions of dislocation core where the absolute value of the Nye tensor density is greatest. This suggests that the region in which segregation energies are substantially less than zero will narrow with increasing pressure. The number of Mg site vacancies created to charge balance the oxidation of Fe^{2+} to Fe^{3+} at high oxygen fugacity increases with total iron content, and the concentration of Mg vacancy defects at dislocation core sites is likely to increase commensurately. However, a full evaluation of the effect of pressure, temperature, and iron content awaits future study.

5. Conclusions

In this paper, empirical interatomic potentials have been used to simulate the segregation of bare and protonated Mg vacancies to dislocation cores in MgO. It was found that the both $V_{Mg}^{''}$ and $2H_{Mg}^{x}$ defects segregate strongly to all three of the major dislocation slip system, with segregation energies up to several electron volts. For all three dislocations, protonated vacancies segregate more strongly than bare vacancies, with the decrease in segregation energy being particularly great for defects around a ½<110>{100} edge dislocation. The presence of the dislocation was found to lift the three-fold degeneracy of the $2H_{Mg}^{x}$ defect, an effect attributed to interactions between the stress field of the dislocation and the anisotropic stress field of the point defect.

The segregation of vacancies (bare and protonated) to dislocation cores in MgO can potentially influence its high-stress rheology, by altering the Peierls stress required to initiate dislocation glide. As we have shown here, vacancy-related defects segregate strongly to all three major dislocation slip systems in this mineral. The calculated binding energies are often considerable, with the lowest energy sites having binding energies of several eV, ensuring that defect concentrations at dislocation cores will be far greater than in the bulk lattice. Consequently, it is possible that dislocation mobility may be enhanced when the chemical environment is suitable for the generation of vacancy-related defects, such as under hydrous or oxidizing conditions. Moreover, vacancies may alter dislocation mobility even for the low (<10 wt ppm H_2O) bulk concentrations of Mg vacancy-related defects characteristic of hydrated MgO, as the large segregation energies mean that vacancies can be three or more orders of magnitude more abundant in the dislocation core than the undeformed bulk lattice at mantle temperatures. Although defects will preferentially segregate to ½<110>{100} edge dislocations, segregation energies are substantially negative for all three major dislocations in MgO.

Acknowledgements

AMW is grateful for support from the UK Natural Environment Research Council (NE/K008803/1 and NE/M000044/1). RS is supported by an Australian Government Research Training Program (RTP) Scholarship. Calculations were performed on the Terrawulf cluster, a computational facility supported through the AuScope initiative. AuScope Ltd is funded under the National Collaborative Research Infrastructure Strategy (NCRIS), an Australian Commonwealth Government Programme. Ian Jackson is thanked for helpful comments made during the preparation of the manuscript. The authors would like to thank Taku Tsuchiya for his editorial handling, and Sebastian Ritterbex and an anonymous reviewer for constructive comments which improved the quality of the manuscript.

References

Amodeo J, Carrez P, Devincre B, Cordier P (2011) Multiscale modelling of MgO plasticity. Acta Materialia 59:2291–2301. doi: 10.1016/j.actamat.2010.12.020

Amodeo J, Carrez P, Cordier P (2012) Modelling the effect of pressure on the critical shear stress of MgO single crystals. Philosophical Magazine 92:1523–1541. doi: 10.1080/14786435.2011.652689

Ashbee KHG, Yust CS (1982) A mechanism for the ease of slip in UO2+x. Journal of Nuclear Materials 110:246–250. doi: 10.1016/0022-3115(82)90152-0

Bilby BA (1950) On the Interactions of Dislocations and Solute Atoms. Proc Phys Soc A 63:191. doi: 10.1088/0370-1298/63/3/302

Bolfan-Casanova N, Keppler H, Rubie DC (2000) Water partitioning between nominally anhydrous minerals in the MgO–SiO2–H2O system up to 24 GPa: implications for the distribution of water in the Earth's mantle. Earth and Planetary Science Letters 182:209–221. doi: 10.1016/S0012-821X(00)00244-2

Bolfan-Casanova N, Mackwell S, Keppler H, et al (2002) Pressure dependence of H solubility in magnesiowüstite up to 25 GPa: Implications for the storage of water in the Earth's lower mantle. Geophys Res Lett 29:89–1. doi: 10.1029/2001GL014457

Bulatov VV, Kaxiras E (1997) Semidiscrete Variational Peierls Framework for Dislocation Core Properties. Phys Rev Lett 78:4221–4224. doi: 10.1103/PhysRevLett.78.4221

Cai W, Bulatov VV, Chang J, et al (2001) Anisotropic Elastic Interactions of a Periodic Dislocation Array. Phys Rev Lett 86:5727–5730. doi: 10.1103/PhysRevLett.86.5727

Cai W, Bulatov VV, Chang J, et al (2003) Periodic image effects in dislocation modelling. Philosophical Magazine 83:539–567. doi: 10.1080/0141861021000051109

Carrez P, Godet J, Cordier P (2015) Atomistic simulations of ½〈1 1 0〉 screw dislocation core in magnesium oxide. Computational Materials Science 103:250–255. doi: 10.1016/j.commatsci.2014.10.019

Cline II CJ, Faul UH, David EC, et al (2018) Redox-influenced seismic properties of upper-mantle olivine. Nature 555:355–358. doi: 10.1038/nature25764

Cordier P, Amodeo J, Carrez P (2012) Modelling the rheology of MgO under Earth/'s mantle pressure, temperature and strain rates. Nature 481:177–180. doi: 10.1038/nature10687

Cottrell AH, Bilby BA (1949) Dislocation Theory of Yielding and Strain Ageing of Iron. Proc Phys Soc A 62:49. doi: 10.1088/0370-1298/62/1/308

Gale JD (1997) GULP: A computer program for the symmetry-adapted simulation of solids. J Chem Soc, Faraday Trans 93:629–637. doi: 10.1039/A606455H

Gale JD, Rohl AL (2003) The General Utility Lattice Program (GULP). Molecular Simulation 29:291–341. doi: 10.1080/0892702031000104887

Gatzemeier A, Wright K (2006) Computer modelling of hydrogen defects in the clinopyroxenes diopside and jadeite. Phys Chem Minerals 33:115. doi: 10.1007/s00269-006-0059-0

Girard J, Amulele G, Farla R, et al (2016) Shear deformation of bridgmanite and magnesiowüstite aggregates at lower mantle conditions. Science 351:144–147. doi: 10.1126/science.aad3113

Hartley CS, Mishin Y (2005a) Characterization and visualization of the lattice misfit associated with dislocation cores. Acta Materialia 53:1313–1321. doi: 10.1016/j.actamat.2004.11.027

Hartley CS, Mishin Y (2005b) Representation of dislocation cores using Nye tensor distributions. Materials Science and Engineering: A 400–401:18–21. doi: 10.1016/j.msea.2005.03.076

Henkelman G, Uberuaga BP, Harris DJ, et al (2005) MgO addimer diffusion on MgO(100): A comparison of ab initio and empirical models. Phys Rev B 72:115437. doi: 10.1103/PhysRevB.72.115437

Hohenberg P, Kohn W (1964) Inhomogeneous Electron Gas. Phys Rev 136:B864–B871. doi: 10.1103/PhysRev.136.B864

Ismail-Beigi S, Arias TA (2000) Ab Initio Study of Screw Dislocations in Mo and Ta: A New Picture of Plasticity in bcc Transition Metals. Phys Rev Lett 84:1499–1502. doi: 10.1103/PhysRevLett.84.1499

Joachim B, Wohlers A, Norberg N, et al (2012) Diffusion and solubility of hydrogen and water in periclase. Phys Chem Minerals 40:19–27. doi: 10.1007/s00269-012-0542-8

Karki BB, Wentzcovitch RM, Gironcoli S de, Baroni S (1999) First-Principles Determination of Elastic Anisotropy and Wave Velocities of MgO at Lower Mantle Conditions. Science 286:1705–1707. doi: 10.1126/science.286.5445.1705

Karki BB, Ghosh DB, Verma AK (2015) First-principles prediction of pressure-enhanced defect segregation and migration at MgO grain boundaries. American Mineralogist 100:1053–1058. doi: 10.2138/am-2015-5143

Katayama I, Karato S (2008) Low-temperature, high-stress deformation of olivine under water-saturated conditions. Physics of the Earth and Planetary Interiors 168:125–133. doi: 10.1016/j.pepi.2008.05.019

Kohn W, Sham LJ (1965) Self-Consistent Equations Including Exchange and Correlation Effects. Phys Rev 140:A1133–A1138. doi: 10.1103/PhysRev.140.A1133

Kröger FA, Vink HJ (1956) Relations between the Concentrations of Imperfections in Crystalline Solids. Solid State Physics 3:307–435. doi: 10.1016/S0081-1947(08)60135-6

Lauzier J, Hillairet J, Vieux-Champagne A, Benoit W (1989) The vacancies, lubrication agents of dislocation motion in aluminium. J Phys: Condens Matter 1:9273. doi: 10.1088/0953-8984/1/47/001

de Leeuw NH (2001) Density Functional Theory Calculations of Hydrogen-Containing Defects in Forsterite, Periclase, and α-Quartz. J Phys Chem B 105:9747–9754. doi: 10.1021/jp0109978

Leslie M, Gillan NJ (1985) The energy and elastic dipole tensor of defects in ionic crystals calculated by the supercell method. J Phys C: Solid State Phys 18:973. doi: 10.1088/0022-3719/18/5/005

Lewis GV, Catlow CRA (1985) Potential models for ionic oxides. J Phys C: Solid State Phys 18:1149. doi: 10.1088/0022-3719/18/6/010

Long MD, Xiao X, Jiang Z, et al (2006) Lattice preferred orientation in deformed polycrystalline (Mg,Fe)O and implications for seismic anisotropy in D″. Physics of the Earth and Planetary Interiors 156:75–88. doi: 10.1016/j.pepi.2006.02.006

Lu G, Kaxiras E (2002) Can Vacancies Lubricate Dislocation Motion in Aluminum? Phys Rev Lett 89:105501. doi: 10.1103/PhysRevLett.89.105501

Madi K, Forest S, Cordier P, Boussuge M (2005) Numerical study of creep in two-phase aggregates with a large rheology contrast: Implications for the lower mantle. Earth and Planetary Science Letters 237:223–238. doi: 10.1016/j.epsl.2005.06.027

Mahendran S, Carrez P, Groh S, Cordier P (2017) Dislocation modelling in Mg 2 SiO 4 forsterite: an atomic-scale study based on the THB1 potential. Modelling Simul Mater Sci Eng 25:054002. doi: 10.1088/1361-651X/aa6efa

Marquardt H, Speziale S, Reichmann HJ, et al (2009) Elastic Shear Anisotropy of Ferropericlase in Earth's Lower Mantle. Science 324:224–226. doi: 10.1126/science.1169365

Miller MK (2006) Atom probe tomography characterization of solute segregation to dislocations and interfaces. J Mater Sci 41:7808–7813. doi: 10.1007/s10853-006-0518-5

Muir JMR, Brodholt JP (2018) Water distribution in the lower mantle: Implications for hydrolytic weakening. Earth and Planetary Science Letters 484:363–369. doi: 10.1016/j.epsl.2017.11.051

Piazolo S, Fontaine AL, Trimby P, et al (2016) Deformation-induced trace element redistribution in zircon revealed using atom probe tomography. Nature Communications 7:10490. doi: 10.1038/ncomms10490

Puls MP (1980) Vacancy-dislocation interaction energies in MgO. Philosophical Magazine A 41:353–368. doi: 10.1080/01418618008239317

Puls MP (1983) Vacancy-dislocation interaction energies in MgO A re-analysis. Philosophical Magazine A 47:497–513. doi: 10.1080/01418618308245242

Puls MP, Norgett MJ (1976) Atomistic calculation of the core structure and Peierls energy of an (a/2) [110] edge dislocation in MgO. Journal of Applied Physics 47:466–477. doi: 10.1063/1.322670

Reddy SM, van Riessen A, Saxey DW, et al (2016) Mechanisms of deformation-induced trace element migration in zircon resolved by atom probe and correlative microscopy. Geochimica et Cosmochimica Acta 195:158–170. doi: 10.1016/j.gca.2016.09.019

Schröder K-P, Sauer J, Leslie M, et al (1992) Bridging hydrodyl groups in zeolitic catalysts: a computer simulation of their structure, vibrational properties and acidity in protonated faujasites (H□Y zeolites). Chemical Physics Letters 188:320–325. doi: 10.1016/0009-2614(92)90030-Q

Shanno DF (1970) Conditioning of quasi-Newton methods for function minimization. Math Comp 24:647–656. doi: 10.1090/S0025-5718-1970-0274029-X

Skelton R, Walker AM (2018) Lubrication of dislocation glide in MgO by hydrous defects. Phys Chem Minerals 45:713–726. doi: 10.1007/s00269-018-0957-y

Stroh AN (1958) Dislocations and Cracks in Anisotropic Elasticity. Philosophical Magazine 3:625–646. doi: 10.1080/14786435808565804

Ventelon L, Lüthi B, Clouet E, et al (2015) Dislocation core reconstruction induced by carbon segregation in bcc iron. Phys Rev B 91:220102. doi: 10.1103/PhysRevB.91.220102

Verma AK, Karki BB (2010) First-principles simulations of MgO tilt grain boundary: Structure and vacancy formation at high pressure. American Mineralogist 95:1035–1041. doi: 10.2138/am.2010.3386

Walker AM, Gale JD, Slater B, Wright K (2005a) Atomic scale modelling of the cores of dislocations in complex materials part 1: methodology. Phys Chem Chem Phys 7:3227–3234. doi: 10.1039/B505612H

Walker AM, Gale JD, Slater B, Wright K (2005b) Atomic scale modelling of the cores of dislocations in complex materials part 2: applications. Phys Chem Chem Phys 7:3235–3242. doi: 10.1039/B505716G

Watson GW, Kelsey ET, Parker SC (1999) Atomistic simulation of screw dislocations in rock salt structured materials. Philosophical Magazine A 79:527–536. doi: 10.1080/01418619908210314

Wolf D, Keblinski P, Phillpot SR, Eggebrecht J (1999) Exact method for the simulation of Coulombic systems by spherically truncated, pairwise r−1 summation. The Journal of Chemical Physics 110:8254–8282. doi: 10.1063/1.478738

Zhang F, Walker AM, Wright K, Gale JD (2010) Defects and dislocations in MgO: atomic scale models of impurity segregation and fast pipe diffusion. J Mater Chem 20:10445–10451. doi: 10.1039/C0JM01550D

Tables

Table 1 Minimum segregation energies (in eV) for point defects around MgO dislocations (1 eV/atom = 96.521 kJ/mol)

	½<110>{110} edge dislocation		½<110>{100} edge dislocation		½<110> screw dislocation	
	channel-centered	ion-centered	O-centered	Mg-centered	channel centered	edge A-centered
$V_{Mg}^{''}$	-1.51	-1.51	-2.84	-3.54	-0.97	-0.98
HPLANE $2H_{Mg}^{x}$	-	-	-4.21	-4.56	-1.35	-0.92
HNORM $2H_{Mg}^{x}$	-	-	-2.96	-2.96	-1.24	-1.27
HCROSS $2H_{Mg}^{x}$	-0.68	-0.71	-	-	-	-
HPARA $2H_{Mg}^{x}$	-2.03	-2.04	-	-	-	-

Figure captions

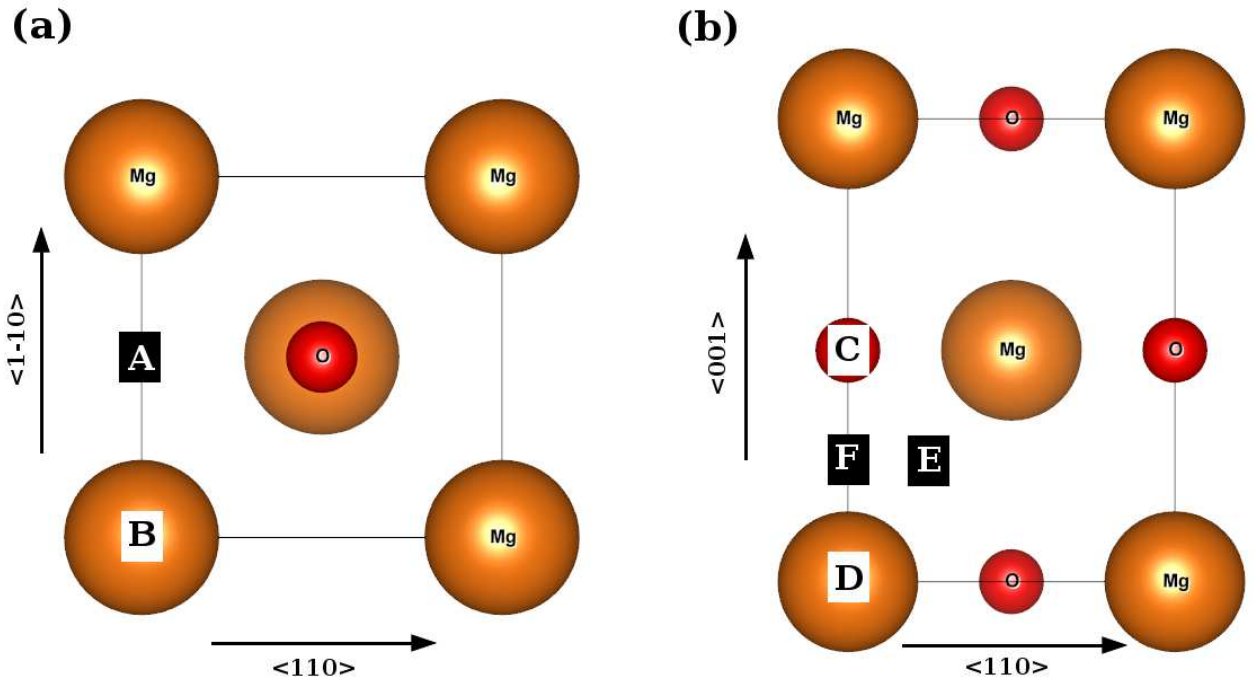

Fig. 1 Crystal structure of MgO, viewed down (a) <100> and (b) <110> with possible high-symmetry dislocation locations marked. The high symmetry locations corresponding to the lowest energy dislocation structures are labeled (from A to F).

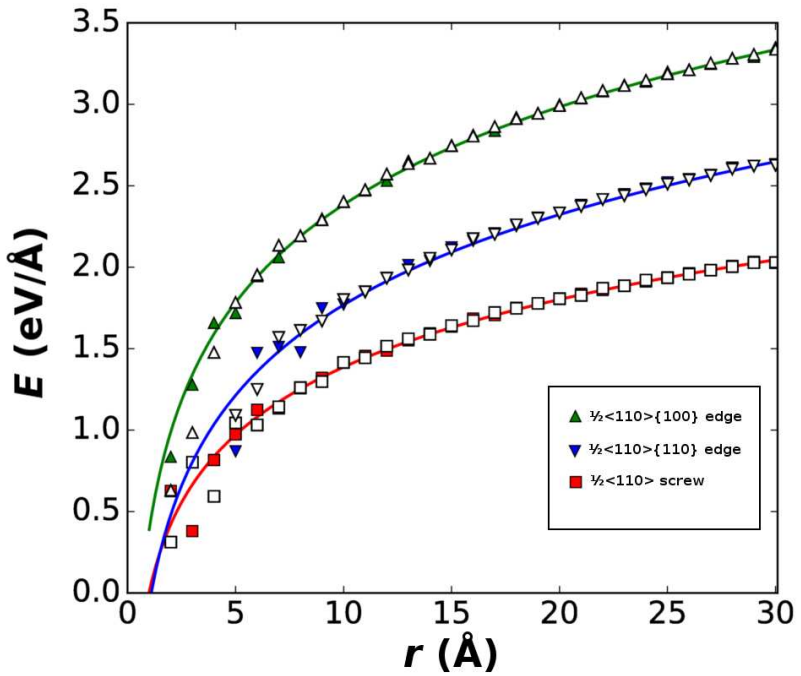

Fig. 2 Radial excess energies $E(r)$ for the lowest core energy polymorphs of the ½<110>{110} (blue inverted triangles) and ½<110>{100} edge dislocations (green triangles), and the ½<110> screw dislocation (red squares). Atomistic energies for <110>-channel-centered ½<110> screw dislocations, ion-centered ½<110>{110} edge dislocations, and Mg-centered ½<110>{100} edge dislocations are shown as filled symbols. Empty symbols denote the atomistic energies of edge A-centered ½<110> screw dislocations, <100>-channel-centered ½<110>{110} edge dislocations, and O-centered ½<110>{100} edge dislocations. Lines show the best fit of equation (1) to the atomistic energies.

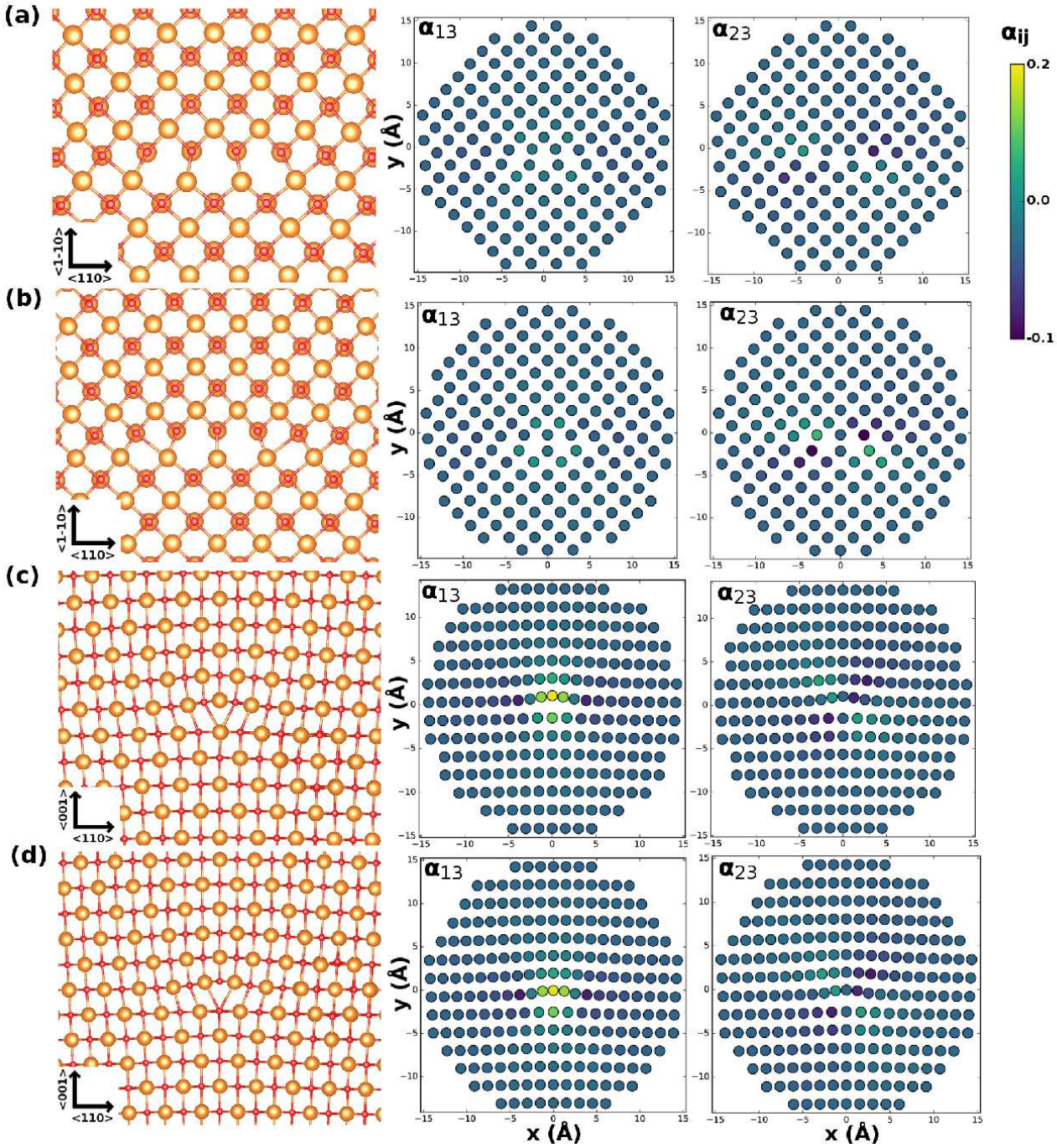

Fig. 3 Atomic structures of the (a) <100>-channel-centered and (b) ion-centered polymorphs of the ½<110>{110} edge dislocation, and of the (c) Mg-centered and (d) O-centered polymorphs of the ½<110>{100} edge dislocation. Also shown are the edge components α_{13} and α_{23} of the Nye tensor $\boldsymbol{\alpha}$.

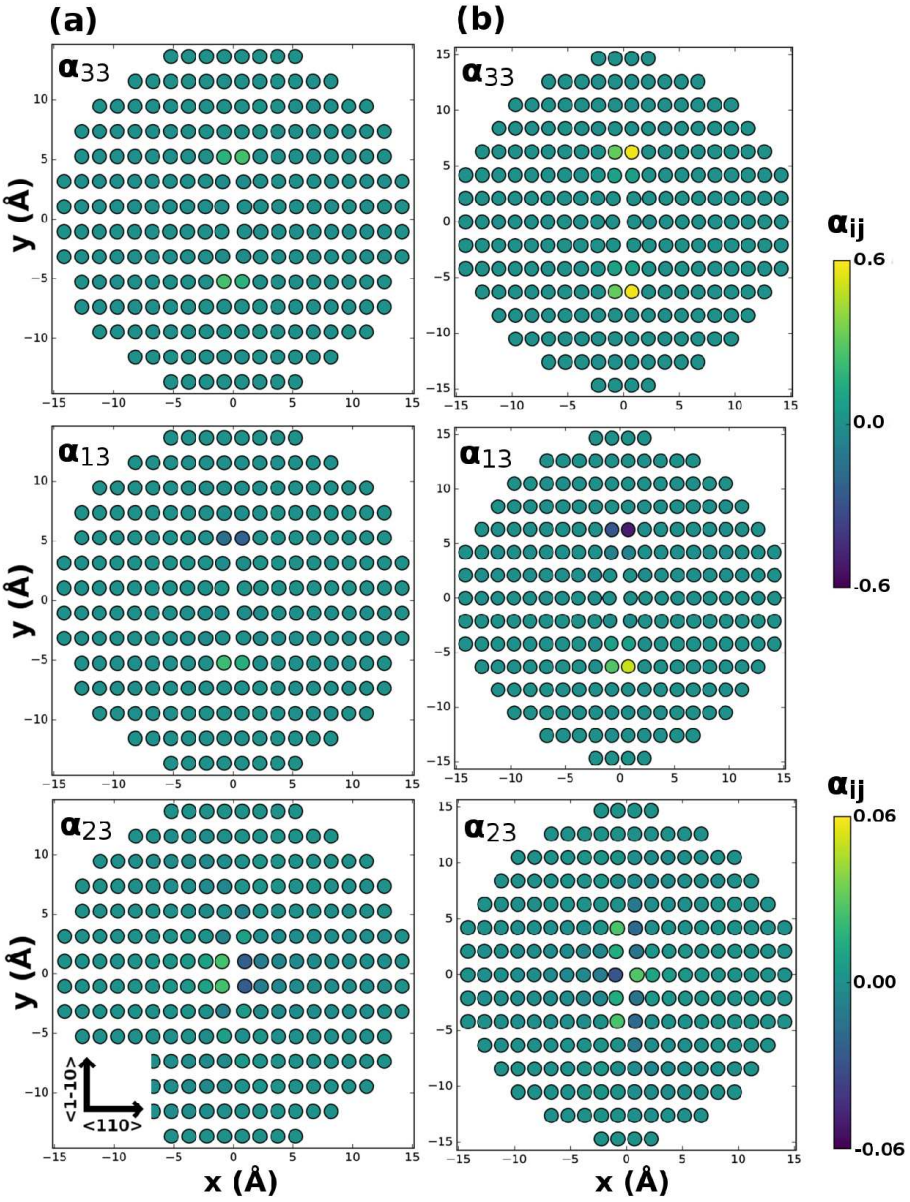

Fig. 4 Screw (α_{33}) and edge (α_{13} and α_{23}) components of the Nye tensor computed for relaxed core structure of the ½<110> screw dislocation in the (a) <110>-channel-centered and (b) edge-A-centered configurations.

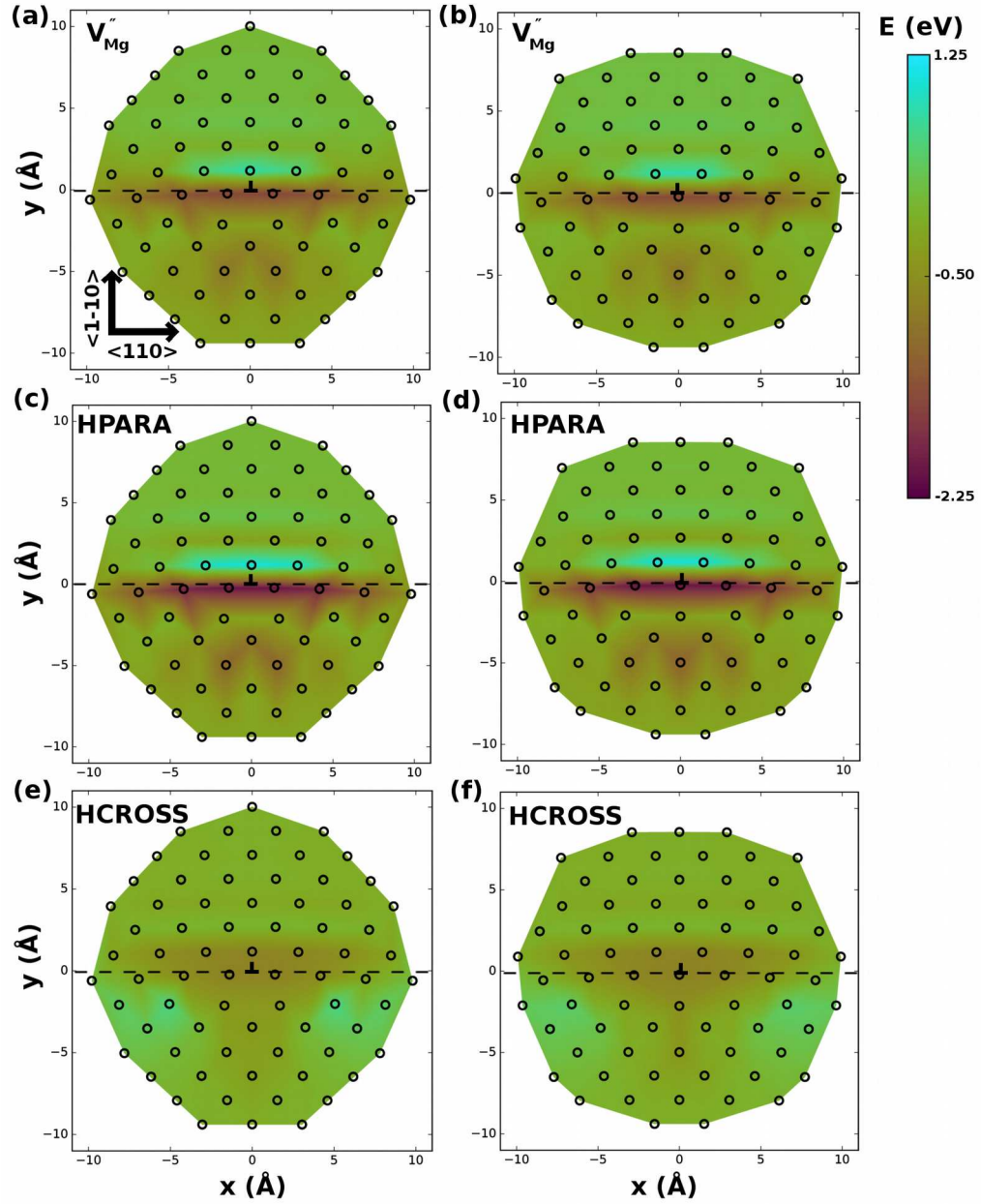

Fig. 5 Energies for segregation of (a, b) V''_{Mg} defects, and $2H^{x}_{Mg}$ defects in the (c, d) HPARA and (e, f) HCROSS configurations to Mg sites around ½<110>{110} edge dislocations. (a), (c), and (e) were calculated using the <100>-channel-centered core structure, while (b), (d), and (f) were calculated using the ion-centered structure. The {110} glide plane has been indicated with a dashed line.

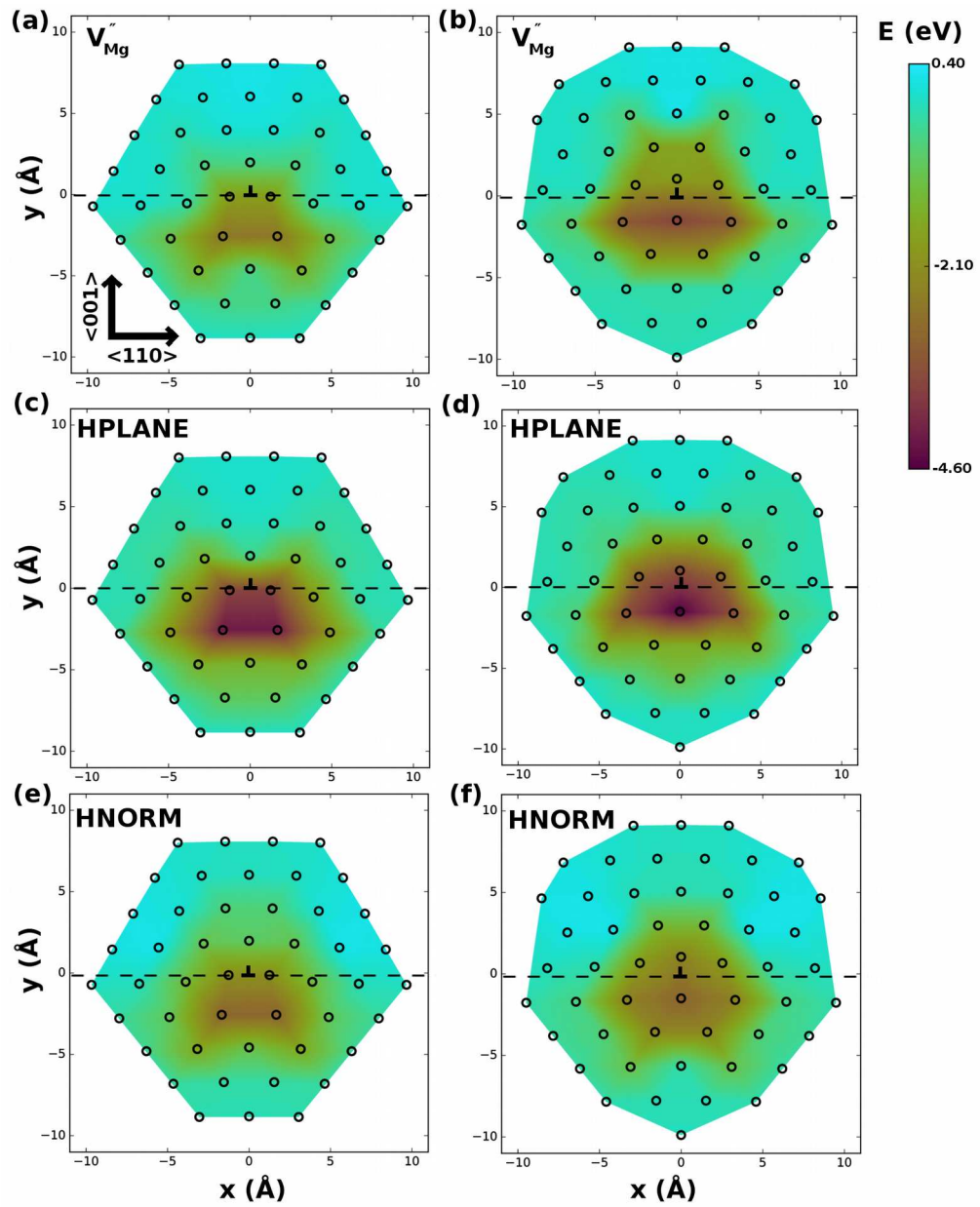

Fig. 6 Energies for segregation of (a, b) V''_{Mg} defects, and $2H^{x}_{Mg}$ defects with the (c, d) HPLANE and (e, f) HNORM configurations to Mg sites around ½<110>{100} edge dislocations. (a), (c), and (e) were calculated for the O-centered core structure, while (b), (d), and (f) were calculated for the Mg-centered structure. The {100} glide plane has been indicated with a dashed line.

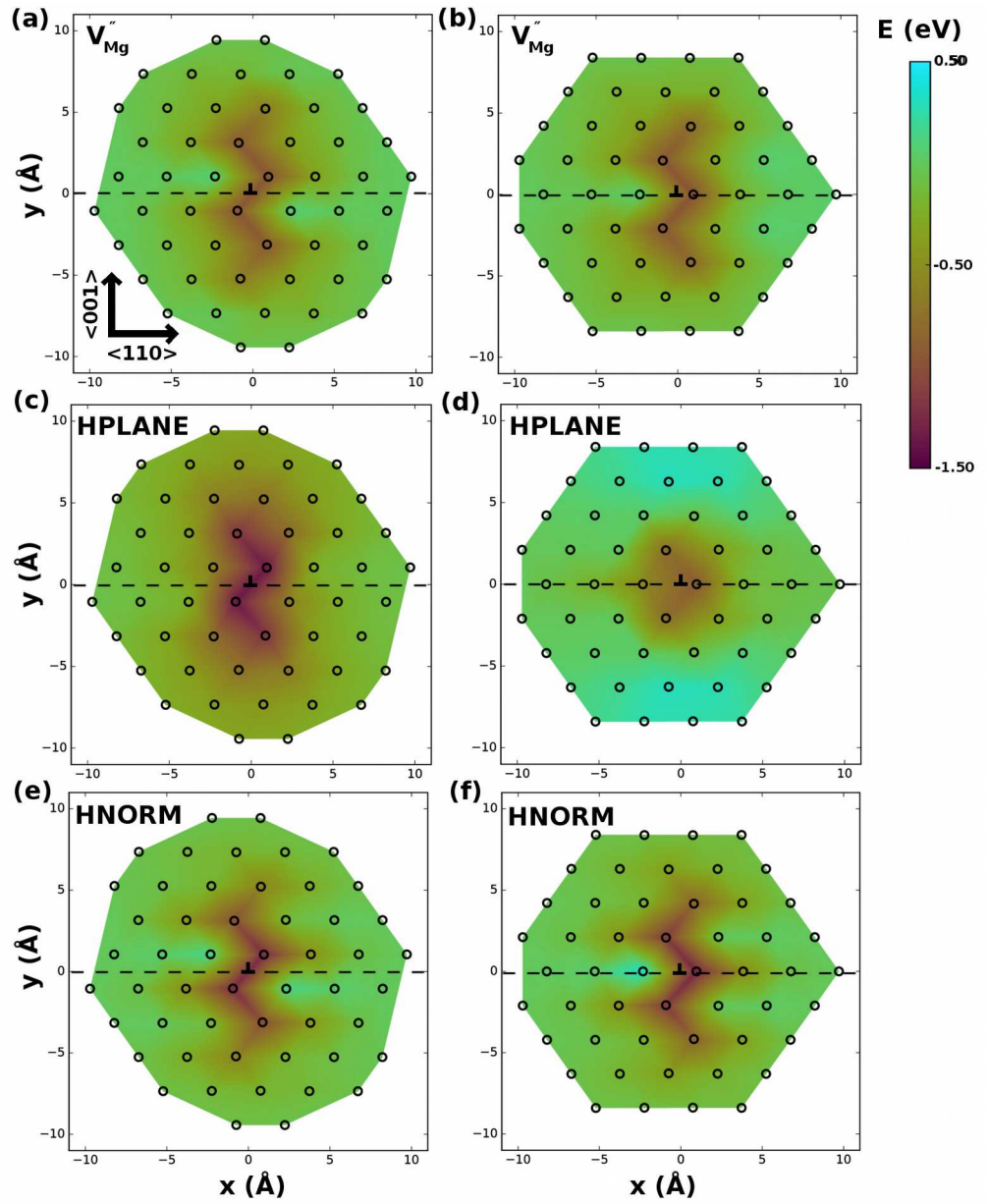

Fig. 7 Energies for segregation of (a, b) V''_{Mg} defects, and $2H^{x}_{Mg}$ defects with the (c, d) HPLANE and (e, f) HNORM configurations to Mg sites around ½<110> screw dislocations. (a), (c), and (e) were calculated for the <110>-channel-centered core structure, while (b), (d), and (f) were calculated for the edge-A structure. The {100} glide plane has been indicated with a dashed line.